Check for updates

Batteries & Supercaps

Research Article
doi.org/10.1002/batt.202400162

Chemistry Europe
European Chemical Societies Publishing

www.batteries-supercaps.org

Advancing Cobalt-Free Lithium-Ion Batteries through Electrochemical Model Refinement and Experimental Parametrization of LNMO | Gr Cells with Gel Polymer Electrolytes

Kato Daems,*[a] Victor Román,[b] Iratxe de Meatza,[b] Elixabete Ayerbe,[b] Kamil B. Dermenci,[a] Joeri Van Mierlo,[a] and Maitane Berecibar[a]

Developing new battery configurations is a time-consuming process, electrochemical models can be employed to expedite the process by predicting the performance of battery designs. An electrochemical pseudo-two-dimensional modeling framework is created for both LNMO | $LiPF_6$ in EC/PC/sulfolane | Gr and LNMO | PVdF GPE with 1.15 M $LiPF_6$ in EC/PC/FEC/sulfolane | Gr configurations with gelifiable electrodes, leveraging the experimental characterization of battery components for enhanced accuracy. Parametrization experiments include quasi-open circuit potential, galvanostatic intermittent titration technique, electrochemical impedance spectroscopy, microscopy and the four-point resistance method. The modeling framework is initiated at full coin cell level and subsequently extended to encompass monolayered, 200 mAh and 500 mAh multilayered pouch cells. Experimental validation, through voltage-capacity measurements, ensures the accuracy of the models. The discharge curves indicate that cells incorporating GPE show similar performance with liquid electrolytes. The impact of increasing current rates on performance is examined by scrutinizing the polarization trends during discharge and the Li-ion concentration in the electrolyte phase. Elevated C-rates induce heightened polarization, detrimentally influencing performance. Importantly, the developed model for full coin cells can be seamlessly expanded to encompass 500 mAh multilayered pouch cells without requiring additional component characterization. This versatility allows the modeling framework to be a valuable tool for evaluating the performance of battery configurations at higher levels.

Introduction

The dependence on fossil fuels is being drastically reduced by the energy transition towards renewable energy sources. Renewable energy sources have inherent variability and intermittency. Unlike conventional fossil fuel energy, which can be adjusted to demand, renewable energy generation is dependent on natural resources.[1] As a result, there are times when renewable energy production may exceed the demand and other times when demand may exceed production. Energy storage systems, including batteries, play a crucial role in managing this variability and ensuring a stable and reliable energy supply. Li-ion batteries (LIBs) are identified as the dominant technology in stationary energy storage applications. The demand for enhanced performance, extended lifespan, and increased safety in LIBs requires the development of novel battery types.[2]

Designing new battery technologies with improved characteristics requires the development of new battery materials. As cobalt is a scarce and costly battery component, with an unethical supply chain, research is conducted towards cobalt-free active materials to improve batteries' economical, ethical and environmental aspects.[3] A potentially cheaper cathode material is $Li_{1.0}Ni_{0.5}Mn_{1.5}O_4$ (LNMO) as it does not contain cobalt. Additionally, LNMO has a high reaction potential (~4.8 V vs Li^+/Li) and high theoretical energy density (~650 Wh/kg).[4,5] High voltage cathodes combined with high capacity anodes like $TiNb_2O_7$ (TNO, theoretical capacity of 388 mAh/g), Si/C composite (theoretical capacity of 3579 mAh/g) or graphite (theoretical capacity of 372 mAh/g) result in batteries with high energy density.[6–8] Commercial batteries contain liquid electrolytes with an ion-conducting lithium salt dissolved in an organic solvent.[9] These organic solvents are volatile, flammable and toxic inducing some severe safety issues due to easy ignition, thermal runaway or explosion. Therefore, the safety of the battery can be significantly improved by eliminating the risk of electrolyte leakage through the application of a semi-solid electrolyte, e.g., a gel polymer electrolyte (GPE).[10–12] GPEs consist of a polymer matrix that encapsulates the liquid electrolyte, serving both as the separator and the electrolyte. In general, the ionic conductivity of GPEs can reach equivalent values as liquid electrolytes and their wettability and mechanical flexibility

[a] K. Daems, Dr. K. B. Dermenci, Prof. J. Van Mierlo, Prof. M. Berecibar
Department of Electromobility Research Centre
Vrije Universiteit Brussel
Pleinlaan 2, 1050 Brussels, Belgium
E-mail: kdaems@vub.be

[b] V. Román, Dr. I. de Meatza, Dr. E. Ayerbe
CIDETEC, Basque Research and Technology Alliance (BRTA)
Paseo Miramón 196, 20014 Donostia-San Sebastián, Spain

Supporting information for this article is available on the WWW under https://doi.org/10.1002/batt.202400162

© 2024 The Authors. Batteries & Supercaps published by Wiley-VCH GmbH. This is an open access article under the terms of the Creative Commons Attribution Non-Commercial License, which permits use, distribution and reproduction in any medium, provided the original work is properly cited and is not used for commercial purposes.

© 2024 The Authors. Batteries & Supercaps published by Wiley-VCH GmbH

Research Article
doi.org/10.1002/batt.202400162
Chemistry Europe
European Chemical Societies Publishing

ensures good solid-solid contact between the electrodes and the gel polymer electrolyte.[12–14]

Nowadays, battery development and optimization are executed via experimental trial-and-error procedures. Consequently, battery development is an extremely costly and time-intensive process. Applying electrochemical models to design, optimize and predict the performance of newly designed battery technologies can significantly reduce this processing time.[15,16] Electrochemical modeling can be a useful tool for understanding, optimizing, and predicting the complex interplay of fundamental processes at the electrolyte-electrode interfaces. The interplay of (electro)chemical reactions and charge transport phenomena within the battery electrodes demands a comprehensive theoretical framework to facilitate a deeper understanding of the mechanisms governing LIB behavior under various operating conditions.[17,18]

Physics-based electrochemical models are based on phenomenological descriptions of cell behavior and can be used to evaluate individual mechanisms happening inside battery cells by predicting internal variables such as the lithium concentration and the electrical potentials.[15,19] The Newman-Doyle Pseudo-two-dimensional (P2D) model is the most commonly used electrochemical model for Li-ion batteries coupling the mass and charge conservations, governed by a set of partial differential equations, as well as electrochemical kinetics.[15,20–22] In practice, numerically solving the computationally complex equations describing the dynamics of a battery cell in all detail over a complete charge/discharge cycle is very costly and time-intensive. Hence, assumptions are made to simplify the mathematical description of a battery cell.[16] The applied assumption of the Newman-Doyle model at the electrode and electrolyte phases includes the porous electrode theory and the concentrated solution theory, respectively.[15,21,23] The P2D model is further simplified by using the volume averaging method (VAM), neglecting the local microstructure and localized current density distribution, and treating the electrodes as a homogeneous medium. The homogeneity simplifications assume that the active material particles in the electrodes are identical spherical particles and are uniformly distributed within the electrodes.[15,24] However, in practice electrodes consist of non-spherical particles, exhibit large dispersity, and porosity and volume fractions vary due to volume changes, crack formation, lithium plating and stress effects during battery cycling. Actual topology and electrode morphology are excluded from the modeling framework. Therefore, the accuracy of the P2D model is limited for predicting cell behavior under extreme conditions.[15] The accuracy of electrochemical models relies on the precise determination of approximately 30 material and electrochemical parameters. Cell analysis is time-consuming and requires specific measuring equipment, consequently being the bottleneck for modeling purposes.[15,25]

This paper introduces a modeling study focused on experimental parameterization and validation of cells incorporating high-voltage LNMO cathodes. These LNMO cells are coupled with either a Microfiber separator loaded with liquid electrolyte (LE, $LiPF_6$ in EC/PC/FEC/sulfolane) or a GPE (gel polymer electrolyte comprising a PVdF polymer matrix and sulfolane-based LE: 1.15 M $LiPF_6$ in EC/PC/FEC/sulfolane) with a graphite anode. The modeling framework is initially developed and validated at the full coin cell level before being scaled up to monolayer pouch cells and multilayer pouch cells with capacities of 200 mAh and 500 mAh. This comprehensive approach allows for a thorough investigation of cell performance and behavior across different configurations and scales, providing valuable insights for battery design and optimization.

Materials and Methods

P2D Model Development

The starting point of the developed modeling framework is the P2D porous electrode model. The Li-ion battery model framework is set up in the thickness direction comprising an anode, a cathode and a separator in three intervals, as depicted in Figure 1. The P2D model includes the concentrated solution theory to describe the transport characteristics in the solution phase, assuming that the electrolyte consists of a binary Li-salt in a single solvent. In the solid electrode phase, the porous electrode theory is used to analyze the composite electrodes. The composite electrodes are composed of electrolyte, solid active material, conductive fillers and binders. The active material particles are spherical with a fixed radius $r_{p,k}$ ($k \in a =$ *anode*, $c =$ *cathode*).[15,21,26]

The porous electrode model is governed by four non-linear partial differential equations (PDE) describing charge- and mass conservations in the electrolyte and the electrodes, combined with one algebraic equation, i.e., the Butler–Volmer equation, to describe the electrode kinetics of the intercalation and de-intercalation reactions at the electrode/electrolyte interface.[17,18,21,24] The governing equations in the developed electrochemical model are presented in the Supporting Information S1. The boundary conditions applied in the model framework describe the electric ground, application of current and the continuity of flux across each boundary.[27]

First, a P2D (pseudo-two-dimensional) model for a full coin cell is developed, comprising five sublayers: Cu-foil, negative electrode active layer, separator, positive electrode active layer,

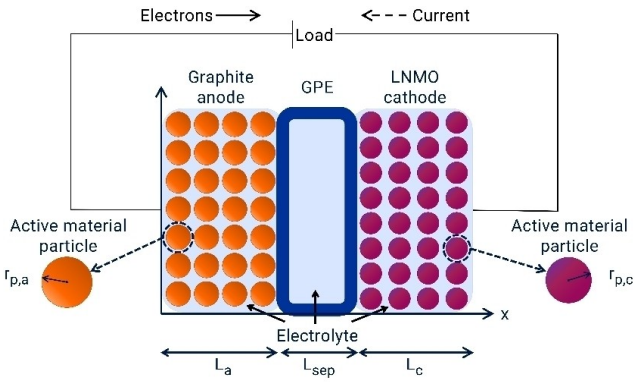

Figure 1. Schematic representation of the Li-ion battery modeling framework in a pseudo-two-dimensional electrochemical model.

© 2024 The Authors. Batteries & Supercaps published by Wiley-VCH GmbH

25666223, 2024, 9, Downloaded from https://chemistry-europe.onlinelibrary.wiley.com/doi/10.1002/batt.202400162 by University of Ulsan, Wiley Online Library on [11/11/2025]. See the Terms and Conditions (https://onlinelibrary.wiley.com/terms-and-conditions) on Wiley Online Library for rules of use; OA articles are governed by the applicable Creative Commons License

Research Article
doi.org/10.1002/batt.202400162
Chemistry Europe
European Chemical Societies Publishing

and Al-foil (refer to Figure 2a). Following model validation against experimental data, primarily focusing on the cell's discharge behavior, this model geometry is extended to a monolayer pouch cell (Figure 2b). This extension involves adjusting the dimensions of the cell components to account for the influence of the cell surface area. Subsequently, the model is further expanded to 200 mAh and 500 mAh multilayered pouch cells, by stacking N unit cells in the following pattern: single-layered anode + separator + double-layered cathode + separator + double-layered anode + … + double-layered cathode + separator + single-layered anode, with N equal to 4 and 10 for the 200 mAh and 500 mAh pouch cells, respectively, as depicted in Figure 2c.

The implementation of the model is done in COMSOL Multiphysics 6.2., a software platform that employs the Finite Element Method (FEM) for the approximation of Partial Differential Equations (PDEs) through discretization.[28]

Among the various approaches, the P2D modelling framework stands out for its high efficiency and accuracy. However, the P2D model requires a significant number of parameters for different cell components, including geometrical, electrochemical and transport parameters. To achieve an accurate simulation of the cell, it is imperative to thoroughly characterize the input parameters of the used cell components. Therefore, the next section is dedicated to the experimental parametrization of the cell components.

Experimental Parametrization

To fully validate the accuracy and robustness of the method presented, validation against experimental results has been conducted. As mentioned earlier, the P2D model is intricate and demands a comprehensive parameterization of the cell to acquire reliable data. Table 1 provides an overview of the cell components characterization techniques employed to determine the parameters required for the P2D model, along with the corresponding estimated parameters. It is worth mentioning that electrolyte properties such as the electrolyte diffusion coefficient, ionic conductivity, and transport number were taken from the literature.

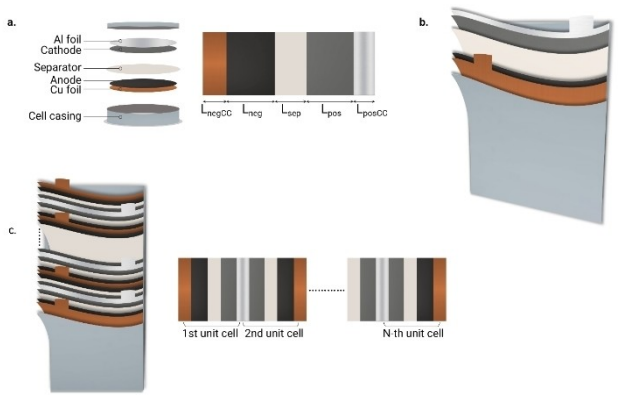

Figure 2. LMNO cell geometries considered for the different cell levels. a. full coin cell level, and b. monolayer pouch cell level, both represented in the model by a single unit cell; c. multilayered pouch cells implemented as N stacked unit cells in the modeling framework.

Sample Preparation

Porous electrodes with a gelifiable PVdF copolymer from Solvay were prepared from slurries with N-methyl-Pyrrolidone (NMP) as solvent. The electrode formulations also comprised carbon black (C-NERGY Super C65 from IMERYS) as a conductive additive, with the following compositions in wt.%: LNMO/C65/PVdF = 90/5/5 (cathode) and Gr/C65/PVdF = 94/2/4 (anode). The cathode loading was 2.0 mAh/cm^2 (1 C = 147 mAh/g-LNMO) while anodes were targeted at 2.2 mAh/cm^2 (1 C = 355 mAh/g-Gr).

As for the electrochemical characterization (EIS, GITT, rate capability) of the components, three different cell configurations were considered. All cells were assembled in an Ar-filled glove box (< 0.1 ppm O2, < 0.5 ppm H2O, Inert, PL-HE-4GB-1950, USA). Pouch cells were assembled in a −42 °C dew point dry room. The different configurations and materials are listed as follows:

Full coin cells (FCC, CR2025) and pouch cells: Working electrode consists of one-sided coated cathode material punched with a high precision cutter at a diameter of 16.6 mm and the counter electrode consists of one-sided coated anode material punched at a diameter of 17.7 mm, both electrodes are separated by the 18.82 mm separator (either the GPE membrane or microfiber). In both cases, 100 μL of liquid electrolyte (LE), with the formulation embedded in the GPE (1.15 M $LiPF_6$ in 20:10:10:60 EC:PC:F1EC:sulfolane), is added to wet and gelify the electrodes. Microfiber (Whatman GF/B) is used as a conventional separator instead of polyolefine-based standards, due to its compatibility and high wettability with the EC:PC:sulfolane electrolyte. The use of this separator allowed us to discriminate the impact of the GPE membrane performance in the full cells. This set-up is used to investigate the rate capability and cycling behavior of the cells and is extrapolated to a larger active area (28.3 cm^2) in monolayer (Figure 2b) and multilayered (Figure 2c) pouch cells used in the validation, as described in section 2.1.

- **Half coin cells (HCC, CR2025)**: Working electrode consists of one-sided coated cathode/anode material punched with a high precision cutter at a diameter of 16.6 mm and the counter electrode consists of Li foil punched at a diameter of

Table 1. Summary of techniques employed in the characterization of the electrodes.

Technique/Equipment	Parameters Estimated
qOCV (Cycler, BaSyTtec)	qOCV, stoichiometries
GITT (Cycler, BaSyTtec)	OCV, diffusion coefficient
EIS (Potentiostat, SOLARTRON)	Exchange current density, tortuosity
Microscopy (FE-SEM, ULTRA plus ZEISS)	Thickness, particle radius
Electronic conductivity probe	Effective conductivity

© 2024 The Authors. Batteries & Supercaps published by Wiley-VCH GmbH

25666223, 2024, 9, Downloaded from https://chemistry-europe.onlinelibrary.wiley.com/doi/10.1002/batt.202400162 by University of Ulsan, Wiley Online Library on [11/11/2025]. See the Terms and Conditions (https://onlinelibrary.wiley.com/terms-and-conditions) on Wiley Online Library for rules of use; OA articles are governed by the applicable Creative Commons License

17.7 mm. As HCC have been assembled to study the intrinsic properties of the electrodes such as the solid diffusion coefficient at the particle level, the 18.82 mm separator employed has always been Celgard 2500 and 100 μL of commercial electrolyte 1 M $LiPF_6$ in 3:7 EC/EMC.

- **Symmetrical coin cells (CR2025)**: Symmetrical cells have been assembled with different electrode configurations, punched at 16.6 mm and with an 18.82 mm Celgard 2500 separator wetted in 100 μL of commercial electrolyte. Both lithium intercalating and blocking electrolytes (1 M $LiPF_6$ in 3:7 EC/EMC and 1 M $TBAPF_6$ in 3:7 EC/EMC) were used for the estimation of kinetic charge constant as well as tortuosity parameter, respectively.

After assembling, all cells except the symmetrical cells, were cycled for two cycles, one at C/20 and one at C/10 to form the SEI. Coin cells showed good reproducibility amongst each other.

Measurement Techniques

In this case, the whole set of parameters listed in Table 2 is determined by the results of experiments performed for the investigated cell material. Thus, all the experimental protocols performed for the estimation of each of the parameters requiring model calibration, as well as validation, are thoroughly described hereafter:

Quasi Open Circuit Potential (qOCP). – Used to obtain the qOCP and stoichiometry ranges. The device employed for the measurement is a BaSyTec CTS, with a voltage accuracy of 1 mV, the temperature is set at 25 °C for the experiments. qOCP is obtained for both the individual electrodes using HCC and the FCC, using 1 M $LiPF_6$ in 3:7 EC/EMC as the electrolyte, to validate the model. As qOCP requires cycling at very slow rates to remain close to equilibrium, currents equivalent to C/50 have been employed.

Galvanostatic Intermittent Titration Technique (GITT). – Used to obtain the solid-state diffusion coefficient. The device employed for the measurement is a BaSyTec CTS, with a voltage accuracy of 1 mV, the temperature is set at 25 °C for the experiments. The GITT has been performed on both the individual electrodes with 1 M $LiPF_6$ in 3:7 EC/EMC electrolyte in HCC after the qOCV C/50 cycling. After being discharged to the minimum voltage, the cells were charged by a stepwise charge process at C/50 and after every 2.5 % SoC the cells were rested for 4 hours, allowing them to reach equilibrium.

Electrochemical Impedance Spectroscopy (EIS). – EIS has been used to identify the exchange current density and tortuosity of the electrodes. The EIS experiments are performed on a potentiostat Solartron 1470E (Solartron Analytical) equipped with an FRA 14558 module. The spectra are obtained with a frequency range of 1 MHz–10 mHz, and with 5 mV amplitude, then they are fitted using ZView software 3.5 (Scribner Associates, Inc). Symmetrical cells are used for all EIS measurements to isolate the resistance contributions of the studied electrode.

Microscopy. – Microscopy is employed to obtain the thickness of the electrodes and separators and the particle radius and its distribution. Measurements were performed on a JEOL JSM 5500LV Scanning Electron Microscope in high vacuum mode with 20 kV electron beam energy and using a secondary electron (SE) detector for sample imaging. Working Distance (WD) was fixed at 15 mm and Spot Size at 35 mm. To avoid drift during image acquisition, the separator was gold sputtered by means of a coater. For anode and cathode imaging, no coating was required as both samples were electron conductive.

Four-point resistance method. – A four-point resistance method is employed to obtain the effective electronic conductivity of the electrodes. For electronic conductivity measurements, the studied electrodes are cut into three rectangular pieces of approximately 2 cm×5 cm. Each sample is weighted and has its thickness measured. The devices employed are a Keithley Model 2400 System SourceMeter which applies a DC current to the outer probes, for the applied currents of up to 100 μA, the resolution of the device is 5 nA, and a Hewlett Packard 34401A multimeter which measures the voltage response on the inner probes, for the measured voltages, the resolution is of 0.005 mV.

Table 2. Physical and geometrical parameters to be implemented in the P2D model.

Parameter	LNMO	GPE	Microfiber + LE	Graphite
Thickness, δ [μm]	64	40	200	49
Initial porosity, ε	0.496	0.01	0.65	0.391
Inactive part	0.1	–	–	0.06
Particle radius, r_p [μm]	4.3	–	–	7.69
Electronic conductivity, σ [$S\,m^{-1}$]	13.67	–	–	291.35
Maximum Li concentration of electrodes, c_{max} [$mol\,m^{-3}$]	24358	–	–	30389
Diffusivity of solid active material, D_s [$m^2\,s^{-1}$]	1.0×10^{-14}	–	–	1.0×10^{-12}
Exchange current density, j_0 [$A\,m^{-2}$]	1.77	–	–	6.53
Li-ion transference number in the electrolyte, t_0^+	–	0.61	0.23	–
Initial electrolyte concentration, $c_{e,0}$ [$mol\,m^{-3}$]	–	1150	1000	–
Electrolyte diffusivity, D_e [$cm^2\,s^{-1}$]	–	6.02×10^{-12}	8.59×10^{-11}	–
Electrolyte conductivity, κ [$S\,m^{-1}$]	–	0.026	0.908	–

© 2024 The Authors. Batteries & Supercaps published by Wiley-VCH GmbH

25666223, 2024, 9, Downloaded from https://chemistry-europe.onlinelibrary.wiley.com/doi/10.1002/batt.202400162 by University of Ulsan, Wiley Online Library on [11/11/2025]. See the Terms and Conditions (https://onlinelibrary.wiley.com/terms-and-conditions) on Wiley Online Library for rules of use; OA articles are governed by the applicable Creative Commons License

Research Article
doi.org/10.1002/batt.202400162
Chemistry Europe
European Chemical Societies Publishing

Results and Discussion

Physical Properties and Parametrization

Following the methodology described in the experimental section of this work the results of the parameterization are shown.

OCP. – The open circuit potential of the individual electrodes has been obtained through qOCV and GITT after a 4 h relaxation test conducted in HCC configuration. Figure 3 illustrates the obtained results. As observed, the GITT results (dashed lines) yield similar outcomes for both charge and discharge cycles. However, even at slow C-rates (C/50), some degree of overpotential for charge and underpotential for discharge is evident, emphasizing the reliance on the GITT results for validation purposes.

Solid diffusion coefficient. – The solid diffusion coefficient is obtained studying the pulses and relaxation of the GITT, the evolution of the voltage during the pulse can be expressed as equation 1:

$$V = Ri_n + \frac{U_0(x_1 - x_s) + U_1(x_s - x_0)}{x_1 - x_0} \tag{1}$$

Where Ri_n is the voltage drop due to resistance R and current i_n, x is the stoichiometry (0: before the pulse, 1: after the pulse, and s: at the particle surface) and U is the equilibrium potential (OCP). For a pulse of duration t, the analytical solution for the stoichiometry at the particle surface for a spherical particle with radius R_p (refer to particle radius determination protocol) corresponds to equation 2:

$$x_s = x_0 - \frac{i_n R_p}{F D_s c_{max}} \left(3\frac{tD_s}{R_p^2} + \frac{1}{5} - 2\sum_{j=1}^{\infty} \frac{1}{\lambda_j^2} \exp\left(-\lambda_j^2 \frac{tD_s}{R_p}\right) \right) \tag{2}$$

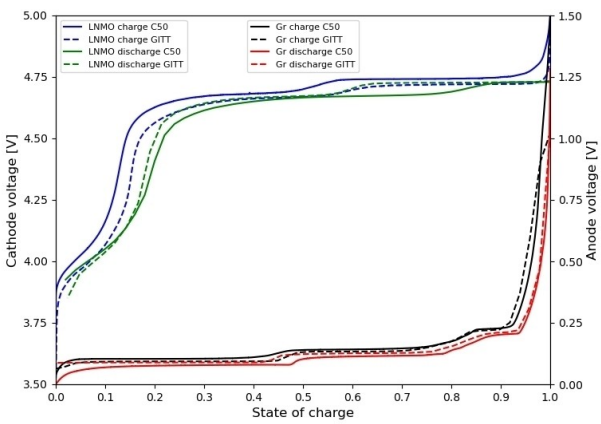

Figure 3. Plot of the individual OCPs of the electrodes obtained through GITT and qOCP at C/50, as can be seen even a C-rate as slow as C/50 still shows some overpotentials, leading to use the GITT results for the OCPs.

where λ_j is an eigen-value function defined as: $\tan(\lambda_j) = \lambda_j$; and c_{max} is the maximum Li concentration in the active material. Therefore, the only unknown parameter in the equation above is the diffusion coefficient, D_s; thus, by fitting the experimental voltage during the pulse with the equations above, the value of D_s can be determined. In this case, the estimated average values for LNMO and graphite are $1.0\times10^{-14}\,m^2\,s^{-1}$ and $1.0\times10^{-12}\,m^2\,s^{-1}$, respectively.

Exchange current density. – The charge transfer kinetics of lithium ions at the electrode can be described by the Butler–Volmer equation, which gives the dependence between the overpotential μ and the current in equation 3:

$$j_n = j_0\left(\exp\left(\frac{\alpha F}{RT}\mu\right) - \exp\left(-\frac{(1-\alpha)F}{RT}\mu\right)\right) \tag{3}$$

where j_0 is the exchange current density and α is the charge transfer coefficient.

An expression for the charge transfer resistance can be obtained by linearising the equation 3 for small values of the overpotential, i.e., around $\mu = 0$. In doing so, it is found that the charge transfer resistance (per electrode), R_{ct}, is related to the exchange current density (j_0) via the following expression (eq. 4):

$$j_0 = \frac{RT}{\alpha F\ S\ R_{ct}} \tag{4}$$

where $R_{ct}$is the charge transfer resistance, obtained from fitting the mid-frequency arc (~ 1 kHz to 1 Hz) in EIS spectra, and S is the reaction surface.

Tortuosity. – Tortuosity is a parameter that reflects the impact of the convoluted and "tortuous" path of the electrode pores on the transport properties of Li-ions in the electrolyte phase. It is defined in various ways to describe its influence, with one common definition involving the MacMullin number, N_M. This parameter illustrates the effect of the pore microstructure on macroscopic observations, as described by the following equation.[29]

$$N_M = \frac{\kappa}{\kappa_{eff}} \tag{5}$$

Which relates the ionic conductivity of the electrolyte solution, κ, to the effective ionic conductivity of a porous membrane, κ_{eff}. The MacMullin number can also be defined as:[30]

$$N_{M_k} = \frac{\tau_k}{\varepsilon_k} \tag{6}$$

Where τ is the tortuosity and ε is the porosity of the electrode/separator and the k subindex denotes the domain. This equation establishes a fundamental relationship for tortuosity based on porosity. Alternatively, tortuosity can also be estimated at a microscopic level by comparing the shortest available path for ions, L_0, to the actual path transversed, L.[31]

© 2024 The Authors. Batteries & Supercaps published by Wiley-VCH GmbH

25666223, 2024, 9, Downloaded from https://chemistry-europe.onlinelibrary.wiley.com/doi/10.1002/batt.202400162 by University of Ulsan, Wiley Online Library on [11/11/2025]. See the Terms and Conditions (https://onlinelibrary.wiley.com/terms-and-conditions) on Wiley Online Library for rules of use; OA articles are governed by the applicable Creative Commons License

Research Article
doi.org/10.1002/batt.202400162
Chemistry Europe
European Chemical Societies Publishing

$$\tau = \frac{L}{L_0} \tag{7}$$

In this work, we determine the tortuosity using equations (5) and (6), which can be rearranged using Ohm's law across a sample with area, A, ionic resistance, R_{ion}, and porosity, κ, and thickness, d. Thus, equation (6) transforms into:

$$\tau = \frac{R_{ion} \cdot \tau \cdot A \cdot \kappa}{d} \tag{8}$$

Particle radius and electrode thicknesses. – The layer thicknesses of the cell components are easy to comprehend and relatively simple to measure, using tools such as calipers or a micrometer. The radii of the active material particles play a crucial role in determining the distance that the intercalated lithium must diffuse to reach the core. Additionally, these radii influence the relaxation time characteristic of solid-phase diffusion, which in turn controls the rate yield. In this context, 2D images obtained by FE-SEM (Figure 4) were processed to extract measurements of layer thicknesses, particle radii, and particle size distributions.

The estimated mean value of the particle radius for both LNMO and graphite was 4.3 μm and 7.69 μm, respectively.

Following the methodology described in the experimental section of this work the results of the parameterization are shown.

Maximum Li concentration in electrodes. – The maximum lithium concentration, c_{max}, that can be stored in the electrode can be calculated using Equation 9:

$$c_{\max} = \frac{z\,\rho_{\mathrm{AM}}}{M_{\mathrm{AM}}} \tag{9}$$

where ρ_{AM} is the density of the material, z is the number moles of Li per mole of active material and M_{AM} the molecular mass or the active material. Once the values of LNMO and graphite are employed we obtain a maximum concentration of 24358 mol m^{-3} for LNMO and 30389 mol m^{-3} for graphite.

Active material volume fraction and porosity – The active volume fraction, of the active material in the electrode, ε_s, is determined using the ratio between the active material volume and the electrode volume Equation 10.

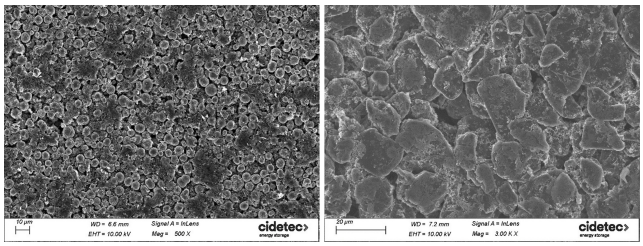

Figure 4. 2D FE-SEM images for both LNMO and Graphite electrodes, used to determine the layer thicknesses, particle radii, and particle size distributions.

$$\varepsilon_s = \frac{\frac{m_e \cdot \%AM}{\rho_{\mathrm{AM}}}}{A_e \cdot t_e} \tag{10}$$

where m_e is the electrode mass, measured on a microbalance, $\%AM$ is the weight percentage of active material, A_e is the electrode area, and t_e its thickness.

The inactive material volume fraction can be calculated using the same formula using the inactive percentage of material. Then the porosity is approximated as the rest of the volume, the values for each one of the volume fractions are shown in Table 2.

Electronic effective conductivity. – In a 4-point system, the current travels away from the probe through the material following cylindrical equipotential shells with a current density given by equation (11)

$$J = \frac{I}{2\pi r t} \tag{11}$$

where r is the radial distance to the probe, t is the thickness of the sample and I the intensity applied through the working probes.

From this point, following Ohm's law and integrating for the distance between the probes, assuming that the thickness of the sample is much smaller than the spacing between the probes one can reach the equation 12:

$$\frac{1}{\sigma} = \rho = \frac{\pi t}{\ln(2)} \frac{V}{I} \tag{12}$$

where ρ is the resistivity, σ the conductivity and V the voltage drop between the sensing probes. Using the previous equation, the conductivity for LNMO and Gr has been determined as 13.7 S m^{-1} and 291.4 S m^{-1}.

For the measurement, the active layer of the electrode was separated from the current collector using double-sided adhesive tape. The tape containing the porous layer was then placed on a stable surface and measurements were performed as described above using the four-point device.

All in all, a summary of the obtained parameters that are introduced in the P2D model framework are presented in Table 2.

Simulation Results and Validation

In order to validate the simulations obtained from the developed modeling framework, charge and discharge tests are carried out at C/5 rate at room temperature. Prior to cycling the full cells undergo a formation process, the testing procedure of these formation cycles is dependent on the composition of the separator. For the cells using a Microfiber separator wetted with 1.15 M $LiPF_6$ in 20:10:10:60 EC:PC:F1EC:sulfolane the formation includes three C/10 cycles. When the gel polymer electrolyte is used the formation consists of one C/20 cycle and one C/10 cycle.

© 2024 The Authors. Batteries & Supercaps published by Wiley-VCH GmbH

25666223, 2024, 9, Downloaded from https://chemistry-europe.onlinelibrary.wiley.com/doi/10.1002/batt.202400162 by University of Ulsan, Wiley Online Library on [11/11/2025]. See the Terms and Conditions (https://onlinelibrary.wiley.com/terms-and-conditions) on Wiley Online Library for rules of use; OA articles are governed by the applicable Creative Commons License

Research Article
doi.org/10.1002/batt.202400162
Chemistry Europe
European Chemical Societies Publishing

Initially, the electrochemical model is developed and experimentally validated for the commercial liquid electrolyte at the coin cell level. This approach is taken to evaluate the performance of the porous electrode model and because the parametrization of the components is performed using coin cells. A comparison between the experimental and simulated voltage profiles for the coin cell configuration, focusing on the initial discharge capacities achieved at a C/5 rate is shown in Figure 5. It can be seen that the model is well able to represent the C/5 discharge behavior of the LNMO|LE|Gr coin cell. The root-mean-square error (RMSE) values are provided in Table 3. We consider the model to be validated since the RMSE value, 18.5 mV, is small, implying that the model has sufficient accuracy to estimate the battery performance.

Therefore, the modeling framework is considered to be experimentally validated at the coin cell level using the commercial liquid electrolyte. The surface area of the porous electrode model is then upscaled to a monolayered pouch cell. The discharge capacity and voltage profile predictions form the simulations, as shown in Figure 5, are compared to experimental tests, revealing a small RMSE of 19.4 mV, which indicated the accuracy of the porous electrode model at the monolayer pouch cell level. Consequently, the model's geometry is further upscaled to multilayered 200 mAh and 500 mAh pouch cells. The voltage profiles for the LNMO|LE|Gr multilayer pouch cells, Figure 5, exhibit small RMSE values of 21.2 mV and 16.6 mV, respectively.

The results from upscaling the models from full coin cell to 500 mAh pouch cell suggest that the modeling parameters, without any further adjustments, determined for a small-scale coin cell can be used to predict the discharge behavior of a large-scale multilayered pouch cell. Making it possible to predict the effect of upscaling of a certain cell configuration, without necessitating further experimental characterizations.

A crucial aspect of evaluating the effectiveness of GPEs involves comparing their performance to state-of-the-art liquid electrolytes. Consequently, the simulations are repeated using the LNMO|GPE|Gr configuration. The performance of the gel polymer electrolyte at various cell levels is detailed in Table 3 and Figure 5. Discharge curves are exclusively provided for simulations that have undergone experimental validation. Thus, only the results for cells using liquid electrolytes are presented for both the full coin and the 500 mAh pouch cells. As seen, the GPE is performing comparably to the established LE in a first cycle. The small difference in achieved capacity can be ascribed to the slightly lower ionic conductivity and consequently, lower Li-ion diffusion coefficient of the GPE when compared to the utilization of a LE, as seen in Table 2. The ion conductivity of GPEs was regarded as a potential limitation because of the solid-like matrix, but the design approaches have successfully addressed this challenge, resulting in conductivity levels that are comparable to liquid electrolytes. The GPE configuration mitigates risks associated with leakage and flammability commonly associated with LEs, preserving the device integrity and safeguarding consumers. The inherent flexibility of gel polymers allows facile incorporation into various device designs, promising versatile applications.

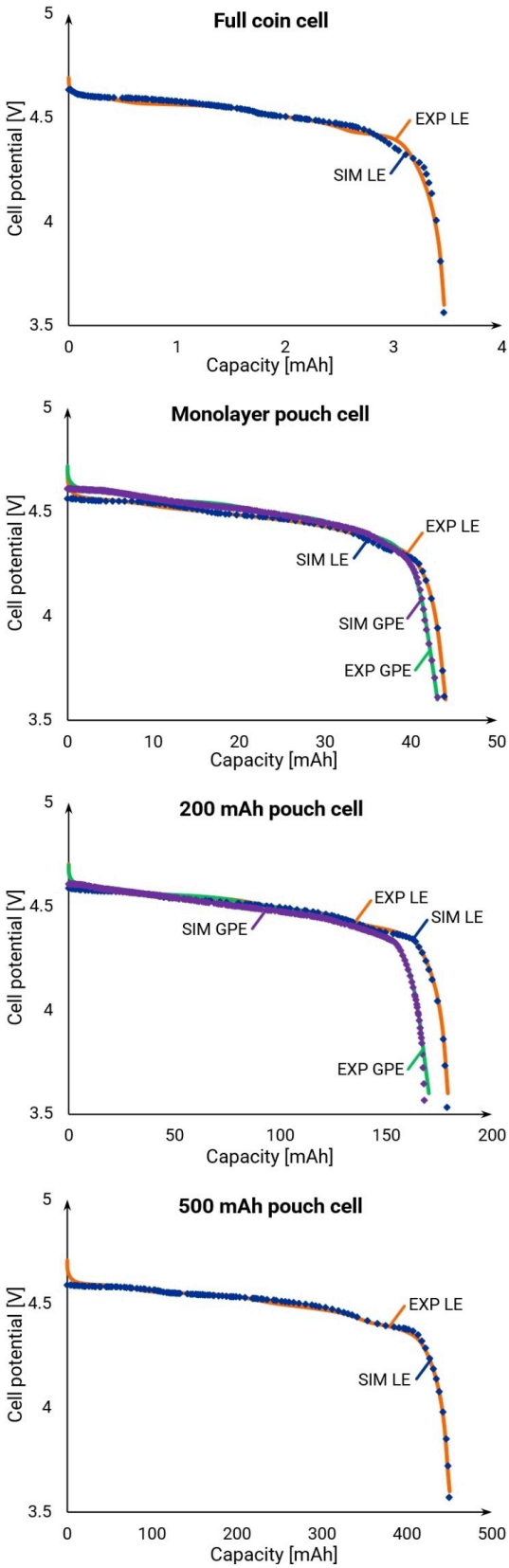

Figure 5. The comparison between experimental and simulated discharge results at C/5 of the full coin cell, monolayer pouch cell, 200 mAh multilayer pouch cell and 500 mAh multilayer pouch cell containing liquid electrolyte or gel polymer electrolyte.

© 2024 The Authors. Batteries & Supercaps published by Wiley-VCH GmbH

25666223, 2024, 9, Downloaded from https://chemistry-europe.onlinelibrary.wiley.com/doi/10.1002/batt.202400162 by University of Ulsan, Wiley Online Library on [11/11/2025]. See the Terms and Conditions (https://onlinelibrary.wiley.com/terms-and-conditions) on Wiley Online Library for rules of use; OA articles are governed by the applicable Creative Commons License

Research Article
doi.org/10.1002/batt.202400162
Chemistry Europe
European Chemical Societies Publishing

Table 3. Discharge capacity of the first C/5 cycle and RMSE values between experimental and simulated results for the cell configurations consisting of LE or GPE at different scales.

Cell configuration		Simulated discharge capacity [mAh]	RMSE [mV]
FCC	LNMO | LE | Gr	3.5	18.5
Monolayer	LNMO | LE | Gr	44.0	19.4
Monolayer	LNMO | GPE | Gr	43.1	22.8
200 mAh	LNMO | LE | Gr	179.1	21.2
200 mAh	LNMO | GPE | Gr	170.0	52.6
500 mAh	LNMO | LE | Gr	450.1	16.6

The non-ideal behavior, i.e., the voltage drop, observed in the discharge curves is caused by polarization. In general, the discharge curves can be divided into three regions, each region with a dominating cause of polarization. At the start of the discharge, a sudden drop in voltage can be observed for the experimental datasets. This immediate decrease in voltage at the start of discharge is caused by Ohmic polarization due to the current flowing across the internal resistance, thereby affecting the charge transfer processes in the battery system. According to Ohm's law, increasing the applied C-rate increases the polarization tendency of the battery.

The developed modeling framework is not able to observe the Ohmic drop at the start of discharge, potentially caused by two factors. Firstly, the one-dimensional geometry of the model assumes that the gradients of the variables are negligible in the directions parallel to the current collectors, therefore missing the potential drop caused by the Ohmic polarization. Therefore, it can be beneficial using a two- or three-dimensional geometry.[32] Secondly, the model assumes the components to be homogeneous, missing the varying particle radii in the electrodes, providing a uniform distribution of potential and potentially missing the effect of polarization.[26] Potential modeling optimization can include the addition of film resistance, accounting for particle size distribution and the non-spherical character of the electrode particles.

The slow voltage decrease of the plateau zone is due to activation polarization related to the kinetics of the electrochemical reactions, i.e., the required overpotential to overcome the activation energy barrier of the electrochemical reaction at the electrode/electrolyte interface, this phenomenon can be described using the Butler–Volmer equation. For this cell configuration the activation polarization is fairly low, as observed by the consistent horizontal trend in the discharge curves, this characteristic is primarily linked to the electrode materials exhibiting a relatively steady voltage profile throughout its entire state of charge, as depicted in Figure 3.

The sharp decrease in voltage at the end of discharge is a result of concentration polarization, originating from the resistance faced by the mass transfer process. The faster consumption of reactants by electrochemical reactions than they diffuse into the porous electrode causes the consumption of Li-ions, consequently causing a drop in their concentration. The difference in Li-ion concentration between the bulk electrolyte and the electrode causes a drop in local potential near the cathode. During the initial part of discharge the concentration polarization is low and it grows rapidly towards the end of discharge and with increasing C-rates, as observed in Figure 6, where the effect of different C-rates on the discharge behavior is depicted.[26,33]

The effect of increasing C-rate on the polarization of the cell can be observed through the decreasing initial cell voltage and voltage plateau, as seen in Figure 6. The Ohmic drop at the initiation of discharge is significantly larger at higher C-rates, e.g., the discharge of 200 mAh pouch cells with GPE at C/5 starts at 4.6 V while a cell potential of 4.4 V is reached for the 2 C current rate. In addition, an increasing slope with increasing C-rate is observed indicating the increase in activation polarization.

The electrolyte salt concentration represents the Li-ion concentration in the electrolyte phase in both the porous electrodes and the separator. The Li-ion concentration in the electrolyte was initially set as 1000 mol/m^3, as observed in Figure 7a at the onset of discharge. Throughout the cell discharge process, the anode consistently maintains a higher Li-ion concentration compared to the cathode. This disparity arises from the initially Li-ion rich state of the anode at the beginning of discharge. As Li-ions deintercalate from the anode active material a higher Li-ion concentration is observed, Li-ions traverse the electrolyte and intercalate into the solid cathode active material particles thus decreasing the Li-ion concentration in the electrolyte phase, resulting in a concentration gradient. This gradient in Li-ion concentration distribution drives Li-ions from the anode to the cathode during the discharge process.

The Li-ion transfer rate in the electrolyte is lower than the deintercalation and intercalation rates. Consequently, the Li-ion concentration within the anode increases, while that within the cathode decreases. The concentration variation is more pronounced during the starting phase of discharge, contrasting with the minimal variation in the middle and end of discharge, suggesting a tendency toward electrolyte concentration stability.[22]

Observably, in Figure 7b, higher C-rates lead to an increase in maximum electrolyte salt concentration and a decrease in

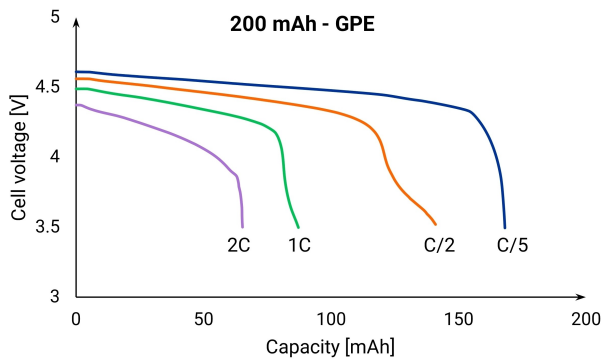

Figure 6. The effect of increasing current rate on the discharge behavior of 200 mAh LNMO | GPE | Gr pouch cells, indicating increasing polarization while applying higher C-rates.

© 2024 The Authors. Batteries & Supercaps published by Wiley-VCH GmbH

25666223, 2024, 9, Downloaded from https://chemistry-europe.onlinelibrary.wiley.com/doi/10.1002/batt.202400162 by University of Ulsan, Wiley Online Library on [11/11/2025]. See the Terms and Conditions (https://onlinelibrary.wiley.com/terms-and-conditions) on Wiley Online Library for rules of use; OA articles are governed by the applicable Creative Commons License

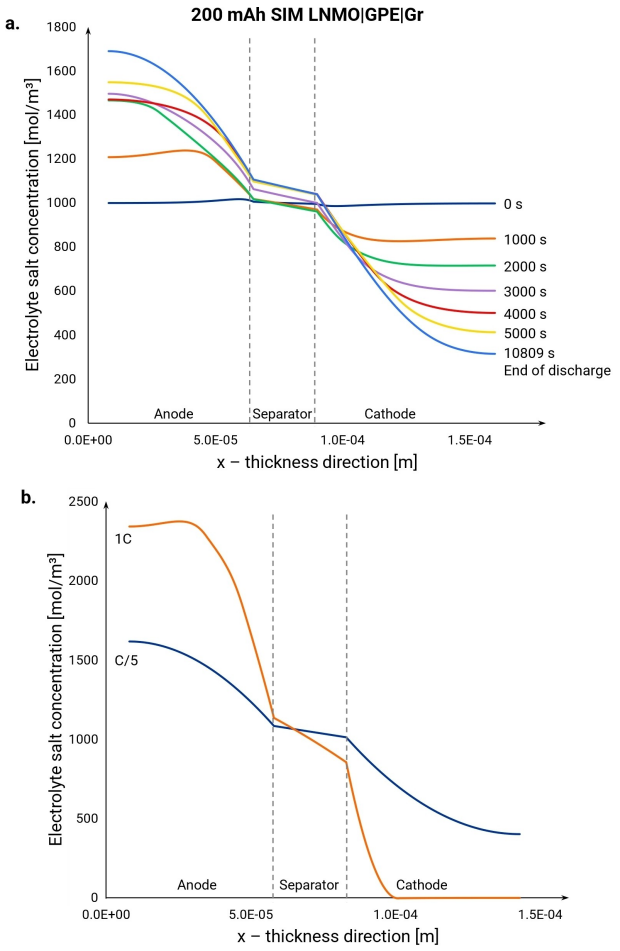

Figure 7. The electrolyte salt concentration profiles along the thickness direction of the cell a. for an applied C/5 current rate at several discharge times, and b. at the end of discharge for C/5, C/2 and 1 C discharge rates.

the minimum, indicating a growing concentration gradient between the electrodes along the thickness direction. At C/5 discharge rate, changes in the concentrations at both ends are only around 500 mol/m^3 whereas, at 1 C the gradient is higher (1000 mol/m^3) resulting in a significant change in the Li-ion concentration in the electrolyte, observed as the steeper slope. This can be attributed to increased polarization with rising C-rates, influencing the diffusion of Li-ions. The electrodes house the electrolyte in their pores, requiring the transportation of lithium ions to the surface of electrode particles through the electrolyte. However, the electrodes and separator possess a certain thickness and porosity, so the electrolyte penetrates into the pore structure inside the electrode with a certain distance and time, thus leading to liquid-phase diffusion polarization. At the end of discharge, higher current rates result in a more depleted electrolyte salt concentration in the cathode, causing an abrupt capacity loss.[22,26]

The P2D-based porous electrode model demonstrates high accuracy in predicting behavior across various cell levels. However, challenges persist, particularly regarding macroscale and microscale assumptions. On the macroscale, the model's limitation to parameters in the thickness direction overlooks in-plane homogeneities, which can be addressed by extending to 2D or 3D models, albeit with increased computational demands. At the microscale, assumptions about identical, spherical electrode particles and uniform Li-ion diffusion do not align with real-world complexities, necessitating enhancements through techniques like topography measurements. Moreover, comprehending the cell cycling behavior requires accurate simulation of battery ageing, hindered by incomplete understanding of all stresses experienced by the cells.[15,26,34]

Conclusions

This paper introduces an electrochemical modeling framework designed to forecast the behavior of LNMO|LE|Gr and LNMO|GPE|Gr cells. At first the model is developed at full coin cell level, involving the characterization of battery components for accurate input parameter integration into the modeling framework. After validation the framework is extended to monolayered and multilayered pouch cells. The first cycle discharge curves suggest that the cells containing GPE are performing comparably to the state-of-the-art liquid electrolyte. Implementing GPEs in battery systems can significantly improve the safety. The discharge curves and Li-ion concentration in the electrolyte phase are further analyzed to observe the impact of varying C-rates on polarization behavior. Higher C-rates induce significant polarization effects, primarily influencing Ohmic- and concentration polarization effects. Experimental discharge curves validate the models at different levels, demonstrating high accuracy across various cell configurations. Importantly, upscaling the modeling framework does not necessitate additional characterization of cell components. This feature enables the prediction of the upscaling effect for a particular cell configuration without the need for extra experimental efforts, thereby significantly reducing the development time for new battery configurations. This study brings an understanding on setting the scene since it extensively covers one of the novel Li-ion chemistries-batteries having gel polymer electrolytes. However, further research is needed to enlighten the aging behavior of such cells.

Acknowledgements

This project has received funding from the European Union's Horizon 2020 Research and Innovation Programme under Grant Agreement No 875126. The authors wish to thank Dominique Bascour from Solvay for the GPE and electrolyte supply as well as Lara Liébana and Ane Muguruza from CIDETEC for the full cell assembly and electrochemical testing.

Conflict of Interests

The authors declare no conflict of interest.

© 2024 The Authors. Batteries & Supercaps published by Wiley-VCH GmbH

25666223, 2024, 9, Downloaded from https://chemistry-europe.onlinelibrary.wiley.com/doi/10.1002/batt.202400162 by University of Ulsan, Wiley Online Library on [11/11/2025]. See the Terms and Conditions (https://onlinelibrary.wiley.com/terms-and-conditions) on Wiley Online Library for rules of use; OA articles are governed by the applicable Creative Commons License

Research Article
doi.org/10.1002/batt.202400162

Chemistry Europe
European Chemical Societies Publishing

Data Availability Statement

The data that support the findings of this study are available from the corresponding author upon reasonable request.

Keywords: Lithium-ion batteries · Electrochemical modeling · Component characterization · Gel polymer electrolytes · Gelifiable electrodes

[1] M. Perrin, Y. M. Saint-Drenan, F. Mattera, P. Malbranche, in *J Power Sources* **2005**, pp. 402–410.
[2] Y. Tian, G. Zeng, A. Rutt, T. Shi, H. Kim, J. Wang, J. Koettgen, Y. Sun, B. Ouyang, T. Chen, Z. Lun, Z. Rong, K. Persson, G. Ceder, *Chem. Rev.* **2021**, *121*, 1623–1669.
[3] Y. Ding, Z. P. Cano, A. Yu, J. Lu, Z. Chen, *Electrochemical Energy Reviews* **2019**, *2*, 1–28, DOI 10.1007/s41918-018-0022-z.
[4] J. Jang, Y. T. Chen, G. Deysher, D. Cheng, S. Y. Ham, A. Cronk, P. Ridley, H. Yang, B. Sayahpour, B. Han, W. Li, W. Yao, E. A. Wu, J. M. Doux, L. H. B. Nguyen, J. A. S. Oh, D. H. S. Tan, Y. S. Meng, *ACS Energy Lett.* **2022**, *7*, 2531–2539.
[5] G. Liang, V. K. Peterson, K. W. See, Z. Guo, W. K. Pang, *J Mater Chem A Mater* **2020**, *8*, 15373–15398.
[6] H. Aghamohammadi, N. Hassanzadeh, R. Eslami-Farsani, *J. Alloys Compd.* **2022**, *911*, 165117.
[7] Y. Ma, P. Guo, M. Liu, P. Cheng, T. Zhang, J. Liu, D. Liu, D. He, *J. Alloys Compd.* **2022**, *905*, 164189.
[8] N. Takami, K. Ise, Y. Harada, T. Iwasaki, T. Kishi, K. Hoshina, *J. Power Sources* **2018**, *396*, 429–436.
[9] C. Li, Z. Wang, Z. He, Y. Li, J. Mao, K. Dai, C. Yan, J. Zheng, *Sustainable Materials and Technologies* **2021**, *29*, e00297, DOI 10.1016/j.susmat.2021.e00297.
[10] S. Chen, K. Wen, J. Fan, Y. Bando, D. Golberg, *J Mater Chem A Mater* **2018**, *6*, 11631–11663.
[11] M. C. Long, T. Wang, P. H. Duan, Y. Gao, X. L. Wang, G. Wu, Y. Z. Wang, *J. Energy Chem.* **2022**, *65*, 9–18.
[12] X. Cheng, J. Pan, Y. Zhao, M. Liao, H. Peng, *Adv. Energy Mater.* **2018**, *8*, 1702184, DOI 10.1002/aenm.201702184.
[13] K. Aruchamy, S. Ramasundaram, S. Divya, M. Chandran, K. Yun, T. H. Oh, *Gels* **2023**, *9*, 585, DOI 10.3390/gels9070585.
[14] H. Jia, H. Onishi, N. von Aspern, U. Rodehorst, K. Rudolf, B. Billmann, R. Wagner, M. Winter, I. Cekic-Laskovic, *J. Power Sources* **2018**, *397*, 343–351.
[15] K. Liu, Y. Gao, C. Zhu, K. Li, M. Fei, C. Peng, X. Zhang, Q. L. Han, *Control Eng Pract* **2022**, *124*, 105176, DOI 10.1016/j.conengprac.2022.105176.
[16] J. Smekens, J. Paulsen, W. Yang, N. Omar, J. Deconinck, A. Hubin, J. Van Mierlo, *Electrochim. Acta* **2015**, *174*, 615–624.
[17] F. Kremer, S. Rael, M. Urbain, *AIMS Energy* **2020**, *8*, 721–748.
[18] S. Sarkar, S. Zohra Halim, M. M. El-Halwagi, F. I. Khan, *J. Electrochem. Soc.* **2022**, *169*, 100501.
[19] A. Falconi, Electrochemical Li-Ion Battery Modeling for Electric Vehicles, Communaute Universite Grenoble Alpes, **2017**.
[20] J. Kim, A. Mallarapu, S. Santhanagopalan, J. Newman, *J. Power Sources* **2023**, *556*, 232413, DOI 10.1016/j.jpowsour.2022.232413.
[21] M. Doyle, J. Newman, *J. Electrochem. Soc.* **1996**, *143*, 1890–1903.
[22] J. Li, Y. Cheng, L. Ai, M. Jia, S. Du, B. Yin, S. Woo, H. Zhang, *J. Power Sources* **2015**, *293*, 993–1005.
[23] Comsol, *The Battery Design Module User's Guide* **2020**.
[24] L. Xia, E. Najafi, H. J. Bergveld, M. C. F. Donkers, *IFAC-PapersOnLine* **2017**, *50*, 2169–2174.
[25] B. Xia, X. Zhao, R. de Callafon, H. Garnier, T. Nguyen, C. Mi, *Appl. Energy* **2016**, *179*, 426–436.
[26] W. Mei, C. Liang, J. Sun, Q. Wang, *Int. J. Energy Res.* **2020**, *44*, 8919–8935.
[27] S. Santhanagopalan, Q. Guo, P. Ramadass, R. E. White, *J. Power Sources* **2006**, *156*, 620–628.
[28] K. K. Pradhan, S. Chakraverty, in *Computational Structural Mechanics* (Eds.: K. K. Pradhan, S. Chakraverty), Academic Press, **2019**, pp. 25–28.
[29] J. Landesfeind, J. Hattendorff, A. Ehrl, W. A. Wall, H. A. Gasteiger, *J. Electrochem. Soc.* **2016**, *163*, A1373.
[30] A. A. Wang, S. E. J. O'Kane, F. B. Planella, J. Le Houx, K. O'Regan, M. Zyskin, J. Edge, C. W. Monroe, S. J. Cooper, D. A. Howey, E. Kendrick, J. M. Foster, *Progress in Energy* **2022**, *4*, 32004.
[31] L. Oca, E. Miguel, E. Agirrezabala, A. Herran, E. Gucciardi, L. Otaegui, E. Bekaert, A. Villaverde, U. Iraola, *Electrochim. Acta* **2021**, *382*, 138287.
[32] U. S. Kim, C. B. Shin, C.-S. Kim, *J. Power Sources* **2009**, *189*, 841–846.
[33] C. Qiu, G. He, W. Shi, M. Zou, C. Liu, *J. Solid State Electrochem.* **2019**, *23*, 1887–1902.
[34] Z. Chen, D. L. Danilov, R.-A. Eichel, P. H. L. Notten, *Adv. Energy Mater.* **2022**, *12*, 2201506.

Manuscript received: March 6, 2024
Revised manuscript received: June 12, 2024
Accepted manuscript online: June 14, 2024
Version of record online: July 29, 2024

© 2024 The Authors. Batteries & Supercaps published by Wiley-VCH GmbH

25666223, 2024, 9, Downloaded from https://chemistry-europe.onlinelibrary.wiley.com/doi/10.1002/batt.202400162 by University of Ulsan, Wiley Online Library on [11/11/2025]. See the Terms and Conditions (https://onlinelibrary.wiley.com/terms-and-conditions) on Wiley Online Library for rules of use; OA articles are governed by the applicable Creative Commons License